Journal of Luminescence 266 (2024) 120316

Contents lists available at ScienceDirect

Journal of Luminescence

journal homepage: www.elsevier.com/locate/jlumin

Full Length Article

Tunable luminescence properties of the $Ca_{3-x}Lu_xSc_{2-x}Mg_xSi_3O_{12}:Ce^{3+}$ phosphor based LD lighting

Xin Li [a], Yu Zhang [a], Hongrui Ren [a], Lunlong Xie [a], Yinsheng Di [a], Mengqing Han [a], Zhaohui Bai [a,**], Quansheng Liu [a,*], Liangliang Zhang [b], Jiahua Zhang [b,***]

[a] School of Materials Science and Engineering, Changchun University of Science and Technology, Changchun, Jilin, 130012, China
[b] Key Laboratory of Excited State Processes, Changchun Institute of Optics Fine Mechanics and Physics, Chinese Academy of Sciences, Changchun, Jilin, 130033, China

ARTICLE INFO

Keywords:
$Ca_{3-x}Lu_xSc_{2-x}Mg_xSi_3O_{12}:Ce^{3+}$
Luminescence properties
Thermal stability
LD light

ABSTRACT

In white-light laser diodes (LD) illumination, the full width at half maximum (FWHM) of the emission spectrum of blue LD is too narrow, leading to the cyan light deficiency, while the emitting color of the material limits the red component of the device. Therefore, in this paper, $Ca_{3-x}Lu_xSc_{2-x}Mg_xSi_3O_{12}:Ce^{3+}$ (CLSMS:Ce^{3+}, x = 0, 0.5, 1, 1.5, 2) phosphor samples were successfully prepared based on $Ca_3Sc_2Si_3O_{12}$ (CSS) cyan-green fluorescent materials with different concentrations of Lu–Mg ions introduced in the matrix instead of Ca–Sc ions. And their luminescence properties were systematically investigated. The peak of the sample was shifted from 508 nm to 590 nm as the concentration of Lu–Mg increased. The thermal stability of the series phosphors gradually deteriorated with increasing Lu–Mg concentration. At 423 K, the emission intensity of the samples was 98.11 %, 94.13 %, 92.18 %, 81.96 % and 77.60 % of that at 298 K, respectively. And the thermal quenching activation energy also gradually decreases. The CLSMS:Ce^{3+} fluorescent materials were prepared into LD devices and tested. It was found that the series of samples showed a gradual decrease in cyan-green light and a gradual increase in red light with increasing Lu–Mg concentration. The CSS compounded with $CaLu_2Mg_2Si_3O_{12}$ (CLMS) obtained a white LD device with color coordinates of (0.3440, 0.3455), and the cyan and red components of the samples were compensated. In summary, this study demonstrates that CLSMS:Ce^{3+} is a very promising fluorescent material to extend the color gamut coverage of fluorescent materials. And it has a potential reference value for the field of white-light LD lighting.

1. Introduction

White light-emitting diode (LED) light source is one of the typical representatives of fluorescence-converting white solid-state light source, which has been widely used in lighting, display and other fields [1]. However, blue LED chips suffer from a severe "efficiency droop" effect, which limits the brightness of the light source [2]. Blue laser diodes (LDs) have no "efficiency droop" compared to LEDs in the field of high power lighting. At the same time, it has the advantages of small size, high brightness, and long life [3–6], which is the key development direction in the field of lighting. Currently, the blue LD excited garnet type $Y_3Al_5O_{12}:Ce^{3+}$ (YAG:Ce^{3+}) yellow fluorescent material is the main way to achieve white light LD lighting [7]. However, the emission spectrum of YAG:Ce^{3+} is mainly covered by yellow-green light, resulting in poor color rendering performance and high color temperature due to the absence of red light in LD light sources [8–10]. In addition, compared with the blue LED chip, the laser chip has a small spot and high power density. When packaged with fluorescent materials, the LD device's light-emitting spectrum is a narrow band of blue light emission [11], making the cyan component of the spectrum missing. Therefore, the green gap effect is also a key factor affecting the improvement of light color quality.

Garnet has a rich structure, and optimisation of the properties of the Ce^{3+} spectrum can be achieved by modifying the ions in the dodecahedral $\{AO_8\}$, octahedral $[BO_6]$ and the tetrahedral (CO_4) site in the $\{A\}_3$ $[B]_2(C)_3O_{12}$ garnet [12]. Therefore, garnet material meet the application requirements of WLD [13], such as $Gd_3Al_5O_{12}:Ce^{3+}$ [14], $Lu_3Al_5O_{12}:Ce^{3+}$ (LuAG:Ce^{3+}) [15–17], $Ca_3Sc_2Ge_3O_{12}:Ce^{3+}$ [18], (Y,

* Corresponding author.
** Corresponding author.
*** Corresponding author.
E-mail addresses: 329073478@qq.com (Z. Bai), liuqs@cust.edu.cn (Q. Liu), zhangjh@ciomp.ac.cn (J. Zhang).

https://doi.org/10.1016/j.jlumin.2023.120316
Received 4 September 2023; Received in revised form 9 November 2023; Accepted 11 November 2023
Available online 17 November 2023

$Lu)_3Al_4GaO_{12}:Ce^{3+}$ [19]. However, most garnet phosphors doped Ce^{3+} ions emit green-yellow light in a wavelength range of 520–550 nm, many strategies to extend the emission range of garnet phosphors are proposed [20–22]. Jia et al. replaced the Lu^{3+}-Al^{3+} ions in LuAG with Mg^{2+}-Si^{4+} ions to obtain $Mg_{1.5}Lu_{1.5}Al_{3.5}Si_{1.5}O_{12}$, which has a similar crystal structure to that of LuAG, and blue-shifted luminescence can be observed [23]. Jiang et al. used Sr^{2+}-Si^{4+} to replace LuAG:Ce^{3+} synchronously to obtain $Lu_{1.5}Sr_{1.5}Al_{3.5}Si_{1.5}O_{12}:Ce^{3+}$ cyan green phosphor. The phosphor has excellent thermal stability (≥60 % retention at 640 K) and is a very promising fluorescent material [24]. Besides this, there are other fluorescent materials, such as $Lu_3(Al,Mg)_2(Al,Si)_3O_{12}$: Ce^{3+} [25], $BaLu_2Al_2Ga_2SiO_{12}$: Ce^{3+} [26], $Y_3MgSiAl_3O_{12}$: Ce^{3+} [27], $Mg_2Y_2Al_2Si_2O_{12}$: Ce^{3+} [28], $Ca_2GdZr_2(AlO_4)_3$: Ce^{3+} [29], $Ca_3Hf_2SiAl_2O_{12}$: Ce^{3+} [30].

Among them, Ca^{2+}-Si^{4+} based garnet is an important substrate for the design of new fluorescent converters [31]. Of all the Ca^{2+}-Si^{4+} based garnet phosphors, $Ca_3Sc_2Si_3O_{12}$ (CSS) has received the most attention. It contains different types of rare earth or/and transition metal ions [32,33]. RE/transition metal CSS mixed crystals doped with Ce^{3+} form this new class. This is a future direction for semiconductor lighting technology [34–40].

Therefore, in this paper, based on CSS:Ce^{3+} matrix, additional Lu^{3+}-Mg^{2+} ion pairs were introduced into CSS:Ce^{3+} garnet hosts to obtain $Ca_{3-x}Lu_xSc_{2-x}Mg_xSi_3O_{12}:Ce^{3+}$ (CLSMS:Ce^{3+}) series fluorescent materials. It turns out that the series of samples has almost the same structure as yttrium aluminum garnet, offering additional possibilities for the modification of the luminescent properties of the materials. Since the CLSMS:Ce^{3+} series materials all belong to the same structure, this provides a research basis for the preparation of cyan-red composite solid-solution fluorescence conversion materials and the development of more efficient phosphor converters. At the same time, it is also shown that this approach can achieve more suitable emission spectrum red-shifts and better color properties than the traditional YAG:Ce^{3+} [41–43], which is a potential reference for the field of white light LD illumination.

2. Experiment

Fluorescence powder preparation. The powder samples of $Ca_{3-x}Lu_xSc_{2-x}Mg_xSi_3O_{12}:0.04Ce^{3+}$ (x = 0, 0.5, 1, 1.5, 2) were prepared by the conventional high-temperature solid-state reaction method. Raw materials were Lu_2O_3 (99.99 %), MgO (A.R.), $CaCO_3$ (A.R.), Sc_2O_3 (99.99 %), SiO_2 (A.R.) and CeO_2 (99.995 %) respectively. Raw materials weighed at the required stoichiometry were mixed and thoroughly ground in an agate mortar. Then, the mixture was transferred to a corundum crucible and sintered at 1350 °C for 4 h in a reducing atmosphere produced by burning the activated carbon. Finally, the samples were cooled to room temperature and the wells were ground for subsequent measurements.

Characterizations. The crystal structure of the sample was tested with an x-ray powder diffractometer (Rigaku, Ultima IV) with a scan range of 10–80° and a scan rate of 5°/min. Fluorescence spectra and decay time were measured by using an Edinburgh fluorescence/lifetime spectrometer. Emission spectra were collected at different temperatures using an RF-5301PC fluorescence spectrometer equipped with a JF-976SS manually controlled heating platform. Diffuse reflectance spectroscopy was performed by using a UV–vis–NIR spectrophotometer. The quantum efficiency was characterized using the C9920-02G quantum efficiency test system, and the sample is placed in an integral ball connected to the instrument, using a 150 W Xe light source. The LD device is used the self-made laser lighting system for testing. It consists of a blue laser diode with an optical power of 80 mW and an integrating sphere, which is connected to the spectrometer (SL-300 photoelectric analyzer integrating sphere produced by ZJU Trichromatic Company) to measure the relevant parameters of the sample.

3. Results and discussion

Fig. 1 shows the XRD pattern of $Ca_{3-x}Lu_xSc_{2-x}Mg_xSi_3O_{12}:0.04Ce^{3+}$ (x = 0, 0.5, 1, 1.5, 2). When x = 0, at which point no Lu–Mg is introduced, the phosphor phase agrees well with the CSS standard card (PDF# 72–1969), indicating that the prepared sample is a pure phase and contains no other impurities. As the value of x increases, more concentrations of Lu–Mg are introduced, causing the CSS phase to begin to fade away. Conversely, the $CaLu_2Mg_2Si_3O_{12}$ (CLMS) phase begins to show up and fits well with the YAG standard card (PDF# 73–1370). However, when the value of x is 2, there are three small diffraction peaks at 29°, 29.4° and 32.2° that matches $YMgSiO_5$ (PDF# 41–0239). Fortunately, the intensity of this small spurious peak is weak and can be seen as having a negligible effect on the lattice structure. Therefore, the Ce^{3+} ions have successfully entered the matrix lattice without being affected by the small amount of heterogeneous phase. In addition to this, the luminous properties of the phosphor are not affected.

On the right is a magnified view of the angular range at 27.2°–34.5°. As can be seen from the graph, the diffraction peak moves towards the higher angles as the x value increases. The reason for this phenomenon is the difference in radius between the substituted ion and the ion being substituted. Ca^{2+} (ionic radius of 1.12 Å, CN = 8) and Sc^{3+} (ionic radius of 0.745 Å, CN = 6) in the matrix are replaced by high concentrations of Lu^{3+} (ionic radius of 0.977 Å, CN = 8) and Mg^{2+} (ionic radius of 0.72 Å, CN = 6). This substitution leads to a shrinkage of the matrix lattice and a reduction in the crystalline surface spacing. According to the Bragg formula [44], the diffraction peaks are shifted in a large angular direction. At the same time, the substitution of Lu–Mg for Ca–Sc changes the lattice constant of the material. It can be seen from equation (1):

$$a = \frac{\lambda\sqrt{h^2 + k^2 + l^2}}{2\sin\theta} \tag{1}$$

Other things being equal, the value of a is inversely proportional to the value of sin θ, and the sin θ is directly proportional to the θ in the range tested. Therefore a and θ are inversely proportional. Where a is the lattice constant, θ refers to the diffraction angle, λ is the X-ray wavelength, and h, k, l represent the Miller index. Thus, as the value of θ increases, the lattice constant a decreases.

In order to further understand the crystal structure of the prepared CLSMS:Ce^{3+} phosphors and to verify the phase purity of the obtained samples, the XRD patterns of the CLSMS:Ce^{3+} series phosphors were refined with Rietveld structure by GSAS software, as shown in Fig. 2(a)–(e). The Rietveld structure parameters of the above refined samples are summarized in Table 1, and the results show that the CLSMS:Ce^{3+} series phosphors are all cubic crystalline isomorphic compounds with the space group Iad (230). The refined structure factor R and χ^2 values are all small, which proves that the results of structural refinement are highly reliable. In addition, the cell volume of YAG is provided in Table 1. By comparison, the cell volume of YAG is smaller than that of CLSMS when x = 0–1.5, however, when x = 2, the cell volume of YAG is larger than that of CLSMS. This result also corresponds to the XRD standard card. The lattice constants, cell volumes, and Ca/Lu/Ce–O coordination bond lengths of the CLSMS:Ce^{3+} samples were obtained by Rietveld refinements and plotted in Fig. 2(f)–(g). It demonstrates the variation pattern of the lattice constant and cell volume of the material, both of which decrease with the increase of Lu–Mg doping. When the doping amount of Lu–Mg is x = 2, the lattice parameter shrinks from 12.2465 Å to 11.9600 Å, which is the same pattern as that calculated in Equation (1) above. This result is also consistent with the occurrence of (4 2 2) crystalline faces shifts at high angles in the XRD pattern in Fig. 1.

Fig. 3(a) shows the crystal structure of CLSMS:Ce^{3+} as simulated by the VESTA software. It can be seen that CLSMS:Ce^{3+} is a cubic crystal system in which the space group is Iad. The CLSMS garnet structure is composed of dodecahedra, octahedra and tetrahedra. In the structure, Lu and Ca are in the dodecahedral position (24c), Mg and Sc occupy the

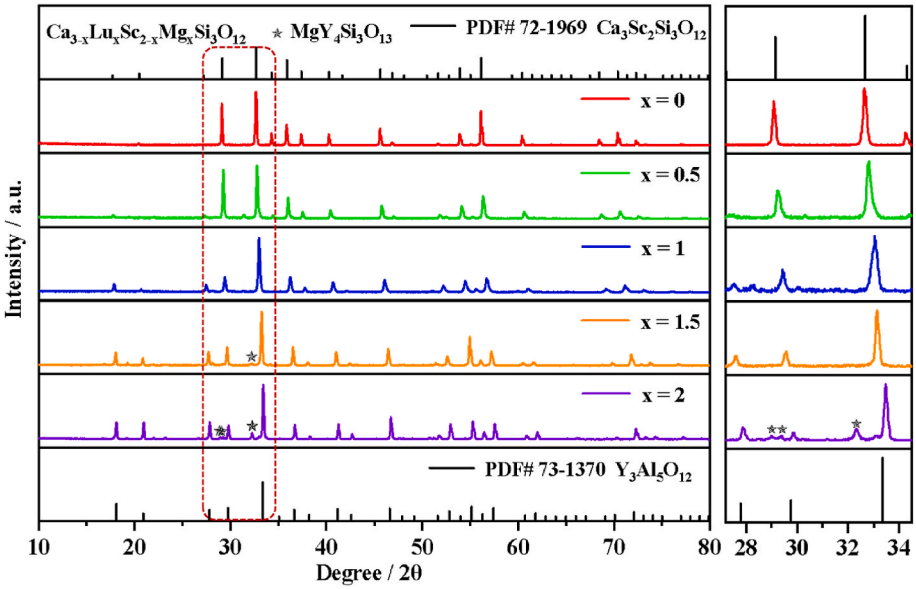

Fig. 1. X-ray diffractogram of $Ca_{3-x}Lu_xSc_{2-x}Mg_xSi_3O_{12}$:0.04$Ce^{3+}$ (x = 0, 0.5, 1, 1.5, 2) fluorescent material (Local magnification of 27.2–34.5° is shown on the right).

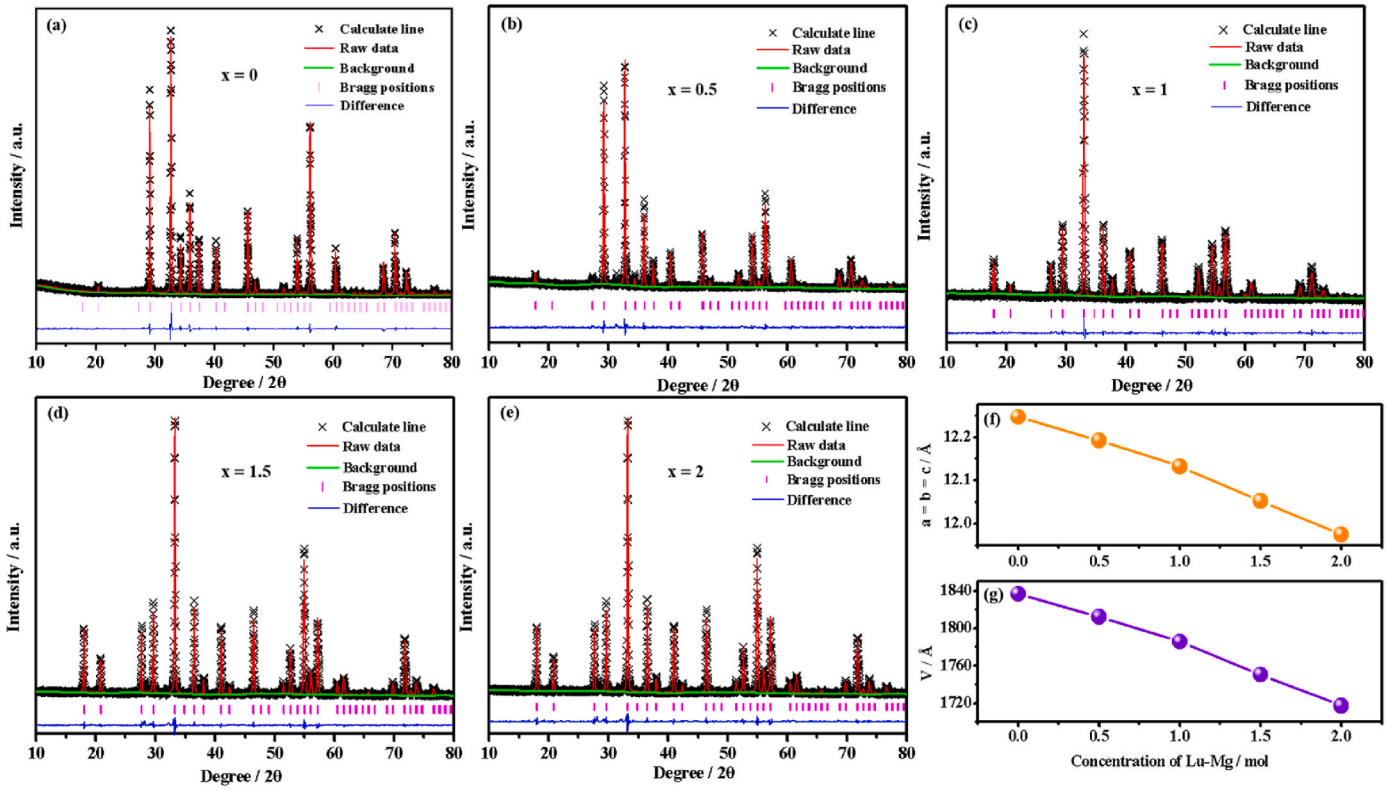

Fig. 2. Rietveld refinements for the XRD pattern of $Ca_{3-x}Lu_xSc_{2-x}Mg_xSi_3O_{12}$:0.04$Ce^{3+}$ (a) x = 0, (b) x = 0.5, (c) x = 1, (d) x = 1.5 (e) x = 2 and variation of (f) lattice constant (g) cell volume.

octahedral position (16a) and Si is in the tetrahedral position (24d). Each [Ca/LuO_8] dodecahedron is connected to four [Sc/MgO_6] octahedra and two [SiO_4] tetrahedra by shared edges. And O atoms connect the [Sc/MgO_6] octahedra and the [SiO_4] tetrahedra. The ionic radius of Ce^{3+} is 1.143 Å (CN = 8) and the ionic radii of Ca^{2+} and Lu^{3+} are 1.12 Å and 0.977 Å (CN = 8), respectively. In the [Sc/MgO_6] octahedral, the ionic radii of Mg^{2+} and Sc^{3+} are 0.72 Å and 0.745 Å (CN = 6), respectively. The ionic radius of Si^{4+} in [SiO_4] tetrahedral is 0.26 Å (CN = 4). Therefore, Ce^{3+} ions are more likely to occupy the lattice position of [Ca/LuO_8], due to their similar ionic radii. Fig. 3(b) demonstrates the variation pattern of the Ca/Lu/Ce–O coordination bond length. It can be seen that with the increase of Lu–Mg doping, the Ca/Lu/Ce–O coordination bond length gradually decreases, which will lead to the gradual deformation of the [$Ca/Lu/CeO_8$] polyhedra occupied by Ce^{3+} and change the crystal field environment of Ce^{3+} to some extent.

The effect of introducing different Lu–Mg concentrations on the luminescence properties of CSS phosphors was further investigated. Fig. 4(a) and (b) show the excitation spectra and emission spectra of

Table 1
The Rietveld structural parameters of $Ca_{3-x}Lu_xSc_{2-x}Mg_xSi_3O_{12}$:0.04$Ce^{3+}$ and YAG [45].

Compound	x = 0	x = 0.5	x = 1	x = 1.5	x = 2	YAG
Space group	Ia $\bar{3}$ d	Ia $\bar{3}$ d	Ia $\bar{3}$ d	Ia $\bar{3}$ d	Ia $\bar{3}$ d	Ia $\bar{3}$ d
Z	8	8	8	8	8	8
a = b = c	12.2465 Å	12.1926 Å	12.1321 Å	12.0519 Å	11.9600 Å	12.0052 Å
α = β = γ	90°	90°	90°	90°	90°	90
Cell volume	1836.68 $Å^3$	1812.53 $Å^3$	1785.70 $Å^3$	1750.54 $Å^3$	1710.78 $Å^3$	1730.27 $Å^3$
R_{wp}	17.54 %	14.71 %	11.75 %	13.26 %	14.12 %	11.34
R_p	13.11 %	11.35 %	9.02 %	9.72 %	10.10 %	8.04
χ^2	1.999	1.871	1.626	2.511	2.778	2.684

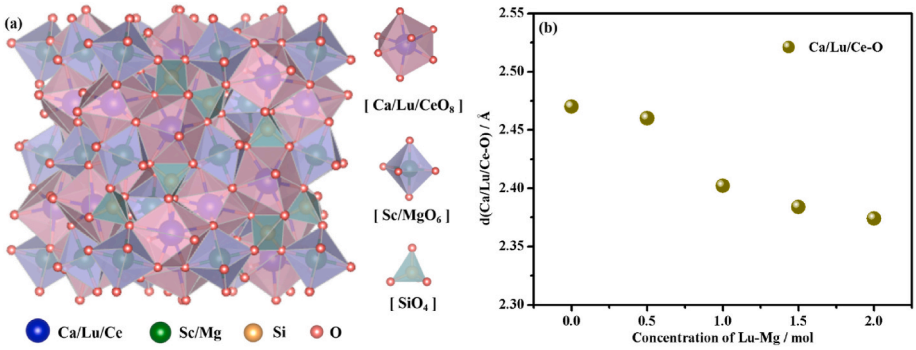

Fig. 3. (a) The crystal structure of CLSMS:Ce^{3+} and (b) Ca/Lu/Ce–O coordination bond length with Lu–Mg concentration in CLSMS:Ce^{3+}.

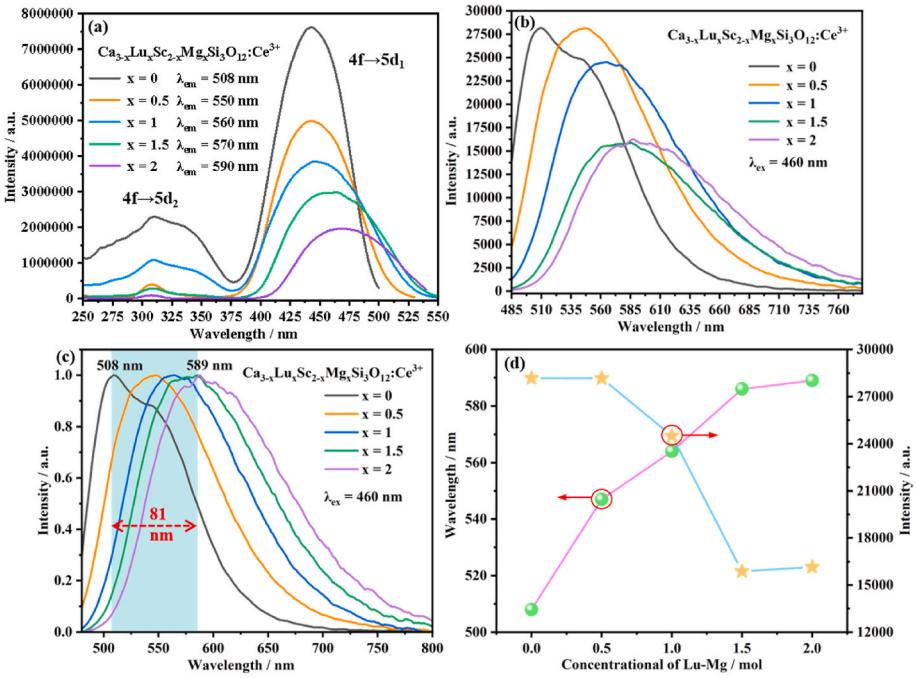

Fig. 4. (a) Excitation spectra, (b) emission spectra, (c) normalized emission spectra of CLSMS:Ce^{3+} materials and (d) trend of emission peak position and luminescence intensity with Lu–Mg value.

CLSMS:Ce^{3+} samples doped with different Lu–Mg concentrations. The shape of the excitation spectra of the CLSMS:Ce^{3+} series phosphors was observed to be essentially the same. They all consist of two broad excitation bands, which are attributed to the transition of the 4f ground state energy level to the 5d excited state of Ce^{3+}. These two lower energy levels arise from the splitting of the energy levels due to crystal field effects. The emission spectra of CLSMS:Ce^{3+} are influenced by the x-value, with different emission intensities and peak positions. The emission spectra of the phosphors show an asymmetric broadband between 485 nm and 760 nm under excitation at 460 nm. This arises from the transition from the 5d lowest excited state energy level of the Ce^{3+} ion to the energy levels of the two 4f ground states ($5d^1 \rightarrow {}^2F_{7/2,\ 5/2}$). The peak position shift pattern of the excitation spectra is similar to that of the emission spectra.

Fig. 4(c) shows the normalized emission spectrum of CLSMS:Ce^{3+}. It can be clearly seen that when Lu–Mg is not introduced, the highest emission peak is located at 508 nm, however when the value of x is increased to 2, the emission peak is at 589 nm. The increase in the value

of x from 0 to 2 shifts the highest emission peak position of the phosphor by 81 nm towards the red light region. The trends of the emission peak position and the luminescence intensity of the CLSMS:Ce^{3+} series phosphors with the concentration of Lu–Mg introduced are plotted in Fig. 4(d). The graph demonstrates that the emission peak position of the phosphor gradually shifts towards larger wavelengths as the Lu–Mg introduction concentration continues to increase.

To further investigate the cause of the red shift of the emission peaks, the Gauss decomposition of the CLSMS:Ce^{3+} (x = 0, 0.5, 1, 1.5, 2) series phosphors were carried out as shown in Fig. 5 (a-e). The figure demonstrates that the broad emission band of each sample can be fitted to two Gauss curves corresponding to the transition from the 5d excited state of the Ce^{3+} ion to the $^2F_{5/2}$ and $^2F_{7/2}$ ground states, respectively. As the Lu–Mg concentration increases, the energy difference between 5d and $^2F_{5/2}$ and $^2F_{7/2}$ gradually decreases. In other words, the energy gap between the lowest excited state energy level and the ground state energy level decreases, resulting in a shift of the emission spectra towards the lower energy side.

From the crystal field environment, the emission spectral redshift is also related to the 5d excited state energy level of Ce^{3+} ions subjected to crystal field splitting effect. It was mentioned earlier that the substitution of Lu–Mg would change the crystal field environment of Ce^{3+} to some extent. The degree of Ce^{3+} crystal field splitting (D_q) can be expressed using equation (2) [46].

$$D_q = \frac{1}{6} Ze^2 \frac{r^4}{R^5} \tag{2}$$

Where D_q refers to the degree of energy level splitting, Z represents the anion charge, e refers to the electronic charge, r is the d-wave number radius and R is the Ce–O bond length. The equation shows that the bond length R of Ce–O is inversely proportional to the degree of crystal field splitting D_q. From Fig. 4(c), it can be seen that the R decreases as the amount of Lu–Mg substitution increases, so D_q becomes larger. In other words, the degree of crystal field splitting increases. As a result, the spectra are red-shifted with the increase of Lu–Mg concentration.

Fig. 6(a) shows the FWHM of the CLSMS:Ce^{3+} material. The FWHM value increases sharply with the increase of x. This is due to the disordered arrangement of Ca^{2+}/Lu^{3+} and Sc^{3+}/Mg^{2+} in the host structure [47]. Fig. 6(b)–(c) shows the CIE chromaticity coordinates of the CLSMS:Ce^{3+} material. In the figure, the red shift due to the change in Lu–Mg concentration can be clearly seen. As shown in Fig. 6(c), the X-coordinate value of the sample gradually increases and the Y-coordinate value gradually decreases as the x-value increases from 0 to 2. Overall, the color coordinates of the sample shift from (0.3224,0.5906) to (0.5199, 0.4739), gradually moving toward the red light. The inset picture of Fig. 6(b) shows the physical photograph of the phosphor. It can be seen that the color of the CLSMS:Ce^{3+} series phosphors changes from cyan-green to orange-red.

Phosphor is subjected to a large amount of heat during the application process, so the thermal stability performance of phosphor is an important indicator for this application. Fig. 7 shows the relative trend of the total emission intensity of CLSMS:Ce^{3+} series phosphors on the emission spectrum intensity at 298 K–523 K. As can be seen from the figure, the emission intensity decreases with increasing temperature due to thermal quenching. It is worth noting that the overall thermal stability of the series phosphors from $Ca_3Sc_2Si_3O_{12}$ to $CaLu_2Mg_2Si_3O_{12}$ becomes progressively worse with increasing Lu–Mg concentration, i.e., the thermal burst gradually increases.

This is due to the multiple interactions between electrons and phonons at high temperatures. It causes a non-radiative phonon-assisted relaxation of the excited state to the ground state, resulting in a decrease in the intensity of the emission spectra. At 423 K, the emission intensity of the samples decrease to 98.11 %, 94.13 %, 92.18 %, 81.96 % and 77.60 % of that at 298 K, respectively.

In general, thermal quenching is mainly due to an increase in the nonradiative relaxation probability and enhance with increasing temperature. This nonradiative relaxation is caused by phonon-electron interactions. The excited-state luminescence center is thermally activated, and a non-radiative relaxation process occurs when the energy of the system rises to the intersection of the ground and excited states. The activation energy of nonradiative relaxation can be calculated using the Arrhenius equation as follows [48]:

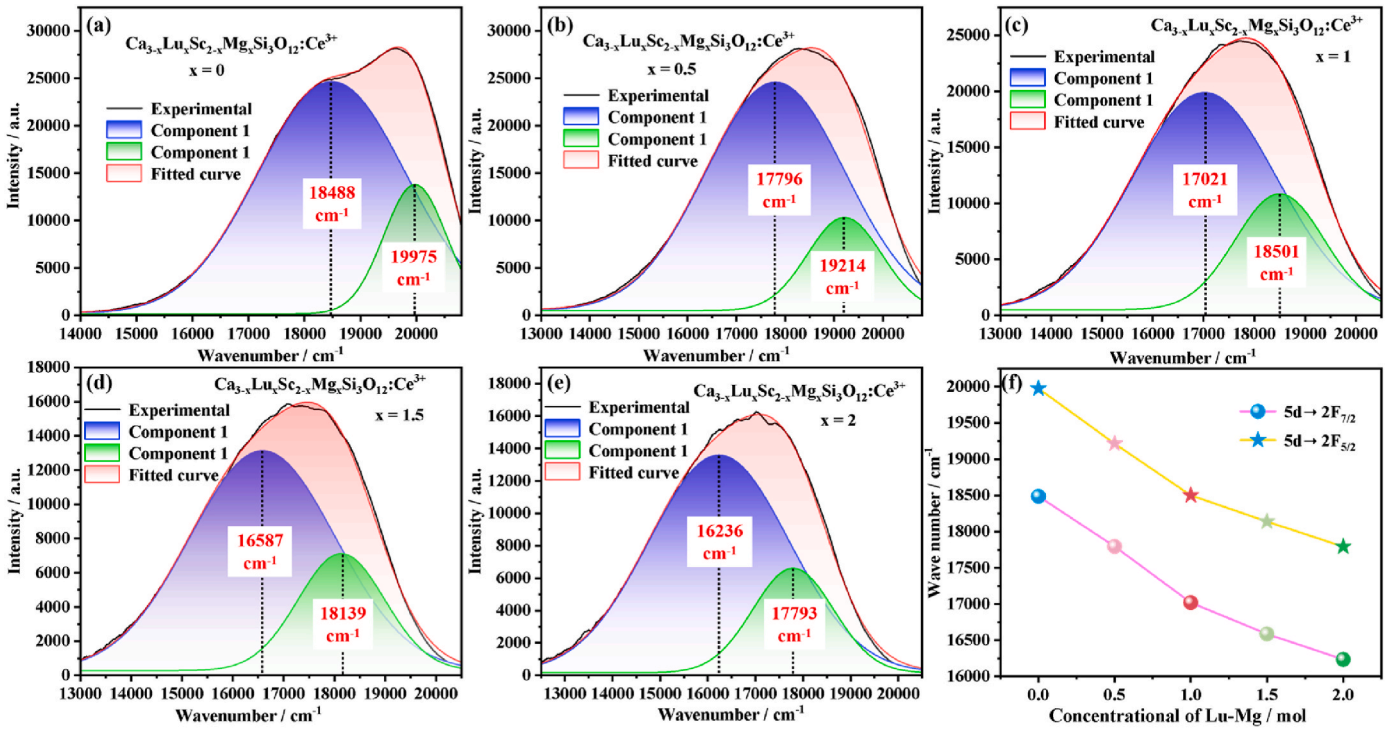

Fig. 5. (a)–(e) The fitted curves of Gaussian splitting peaks for CLSMS:Ce^{3+} materials and (f) the variation of energy difference between $5d^1$ and $^2F_{5/2}$, $^2F_{7/2}$.

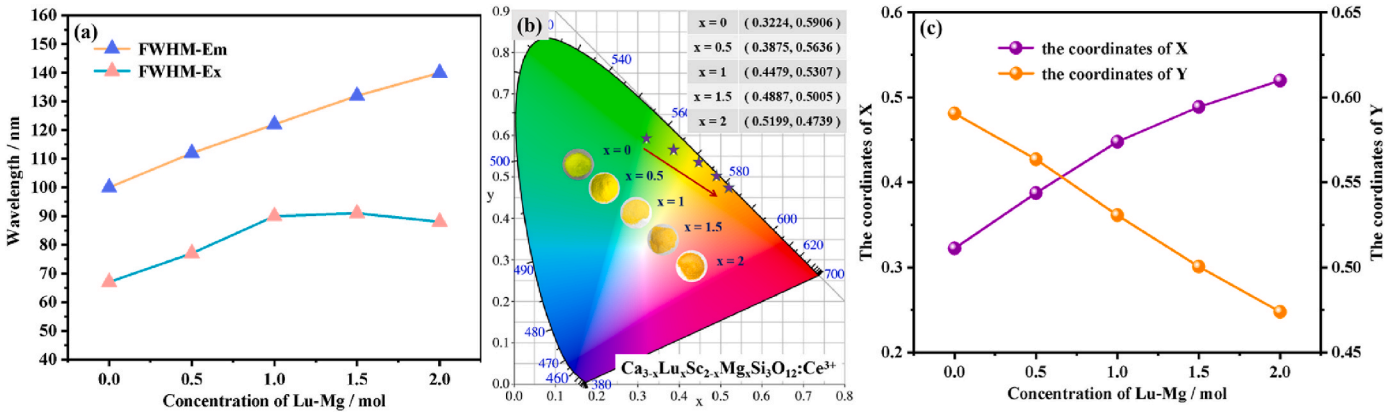

Fig. 6. (a) FWHM, (b) the CIE coordinate coordinates of CLSMS:Ce^{3+} series materials (The inset diagram shows the physical photographs of the phosphors) and (c) the trend diagram of X and Y coordinate values with the introduction of Lu–Mg.

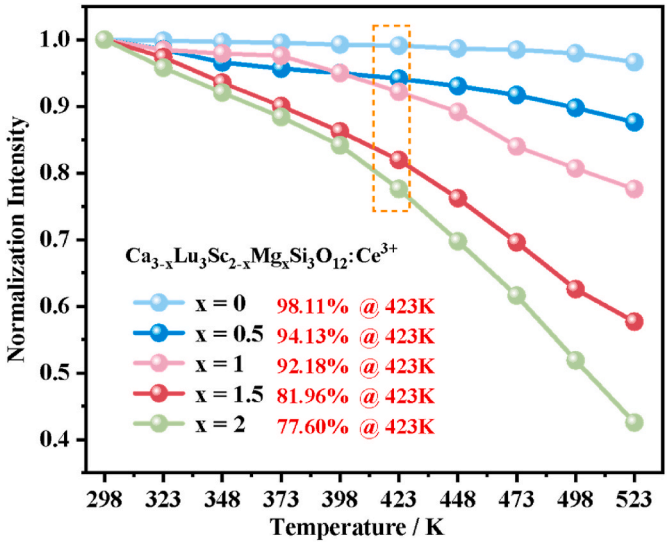

Fig. 7. Normalized intensity of CLSMS:Ce^{3+} materials as a function of temperature.

$$I_T = \frac{I_0}{1 + C\,exp\left(-\frac{\Delta E}{kT}\right)} \tag{3}$$

Where I_0 represents the initial emission intensity, I_T refers to the emission intensity at different temperatures, T is the absolute temperature, C is a constant, ΔE is the activation energy, and k is the Boltzmann constant (8.617×10^{-5} eV K^{-1}). A higher activation energy also implies a better thermal stability. The ln (I_0/I_T-1) and 1/kT for each temperature were traced and linearly fitted, and the activation energy was obtained from the slope of the linear fit curve. According to the calculations, as shown in Fig. 8(a)-(e), the thermal quenching activation energies of CLSMS:Ce^{3+} phosphors are 0.3347 eV, 0.2195 eV, 0.3342 eV, 0.2389 eV and 0.2368 eV, respectively. The results show that the thermal stability decreased with the increase of Lu–Mg concentration. This phenomenon is the thermal cross-relaxation of Ce^{3+} ions from $5d_1$ to 4f level, which can be interpreted in terms of a configuration coordinate diagram, as shown in Fig. 8 (f). When the Lu–Mg concentration increases, the emission spectrum is red-shifted and $\Delta R_3 > \Delta R_2 > \Delta R_1$. With the increasing temperature, the luminous ions in the excited state make a thermal activated transition back to the ground state at the intersection of the ground state and the excited state, and thus the thermal quenching activation energy of the material is reduced ($\Delta E_3 < \Delta E_2 < \Delta E_1$), which is consistent with the experimental results.

In addition, the thermal quenching phenomenon of Ce^{3+} can be explained in another way. The main band gap (E_g) is thought to play an important role in the thermal quenching of photoluminescence. To ensure to clarify the relationship between the thermal quenching of the photoluminescence and the band gap width. The UV–visible diffuse reflectance of the CLSMS series phosphors was measured in Fig. 9, and the phosphor band gaps are approximated to be 3.01 eV, 2.92 eV, 2.90 eV, 2.85 eV and 2.78 eV. It follows that the band gap width of the host lattice gradually becomes smaller as the Lu–Mg concentration increases. This change will result in a decrease in the distance between the 5d energy level of Ce^{3+} and the conduction band. As its gap gets narrower, the quenching of photoluminescence is stronger when the temperature rises. In other words, when the Ce^{3+} ions transition from the 4f ground state to the 5d energy level, the excited electrons couple to the phonons, and the probability of the excited electrons entering the conduction band through thermal ionization will increase. As the number of electrons undergoing a nonradiative transition increases, the luminescence intensity also decreases. However, the nonradiative relaxation caused by the phonon-electron interaction plays a major role due to the small change in the main band gap.

In addition to thermal stability, quantum yield (QY) is an important parameter used to evaluate samples in practical applications. QY can be calculated according to equation (4):

$$\eta_{QY} = \frac{\int L_S}{\int E_R - \int E_S} \tag{4}$$

Here, the L_S refers to the emission spectra of the test sample. E_R refers to the spectrum of excitation light in the absence of a sample in the integration sphere, while E_S is the spectrum of the excitation light in the presence of the sample. The QY of CLSMS:Ce^{3+} series samples were tested at 450 nm as the excitation wavelength. The final phosphor QY values are obtained with x from 0 to 2 corresponding to 93 %, 83 %, 73 %, 71 % and 66 %, respectively. It is confirmed that the CLSMS series samples are a good matrix material for Ce^{3+} ions doped phosphors.

Fig. 10 shows the luminescence decay curves of CLSMS:Ce^{3+} series phosphors, and the decay time of the phosphors was calculated using a double exponential function fit. The fitting equation is as follows:

$$I = A_1\,exp(-t/\tau_1) + A_2\,exp(-t/\tau_2) \tag{5}$$

where I refers to the luminous intensity, τ denotes the lifetime, and A denotes the fitting parameter. In Fig. 10(a), the Ce^{3+} fluorescence decay time shows a downward trend, indicating that there is an easier nonradiative escape pathway during the electron transition. This will also limit the improvement of its luminescence intensity and thermal stability energy, and then reduce the quantum efficiency. Fig. 10(b) shows

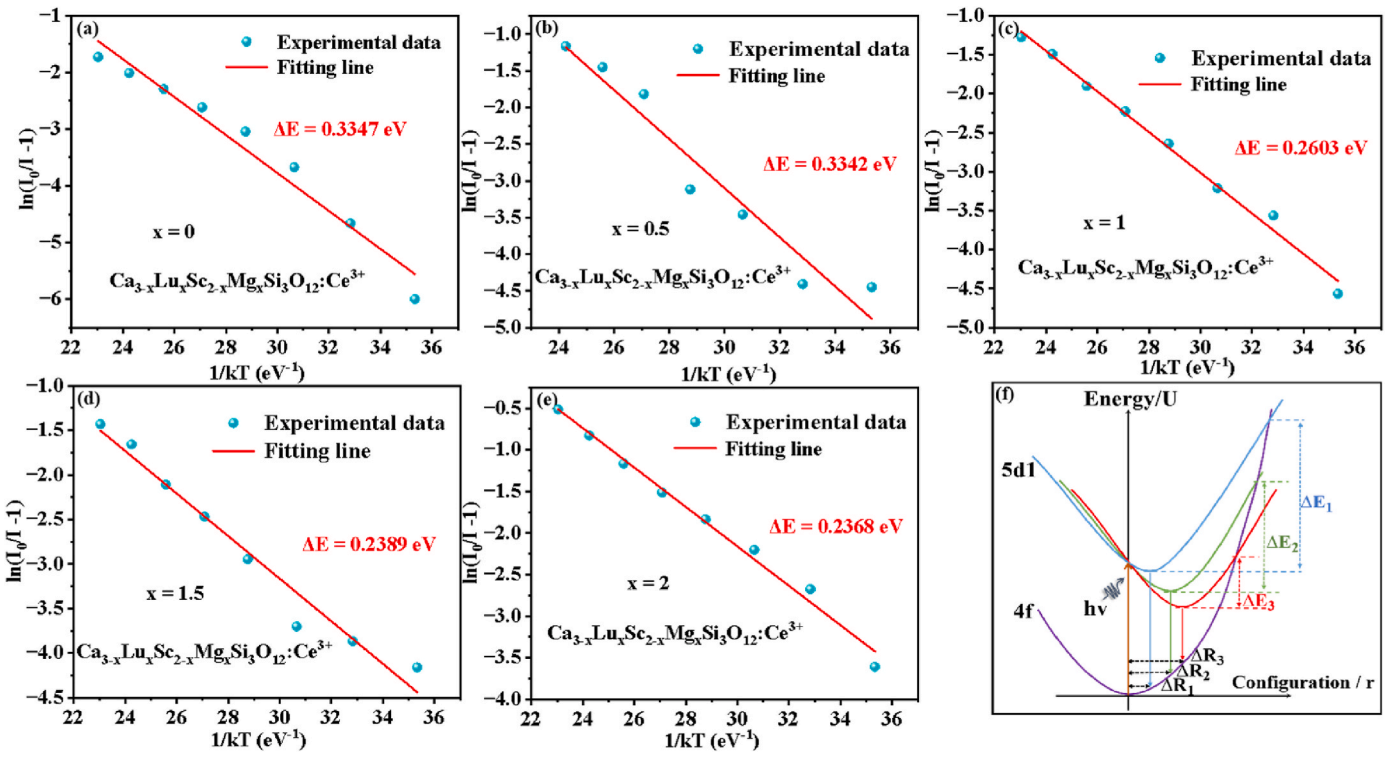

Fig. 8. (a)–(e) Plot of ln (I_0/I-1) and 1/kT in CLSMS:Ce^{3+} samples and (f) configuration coordinate diagram.

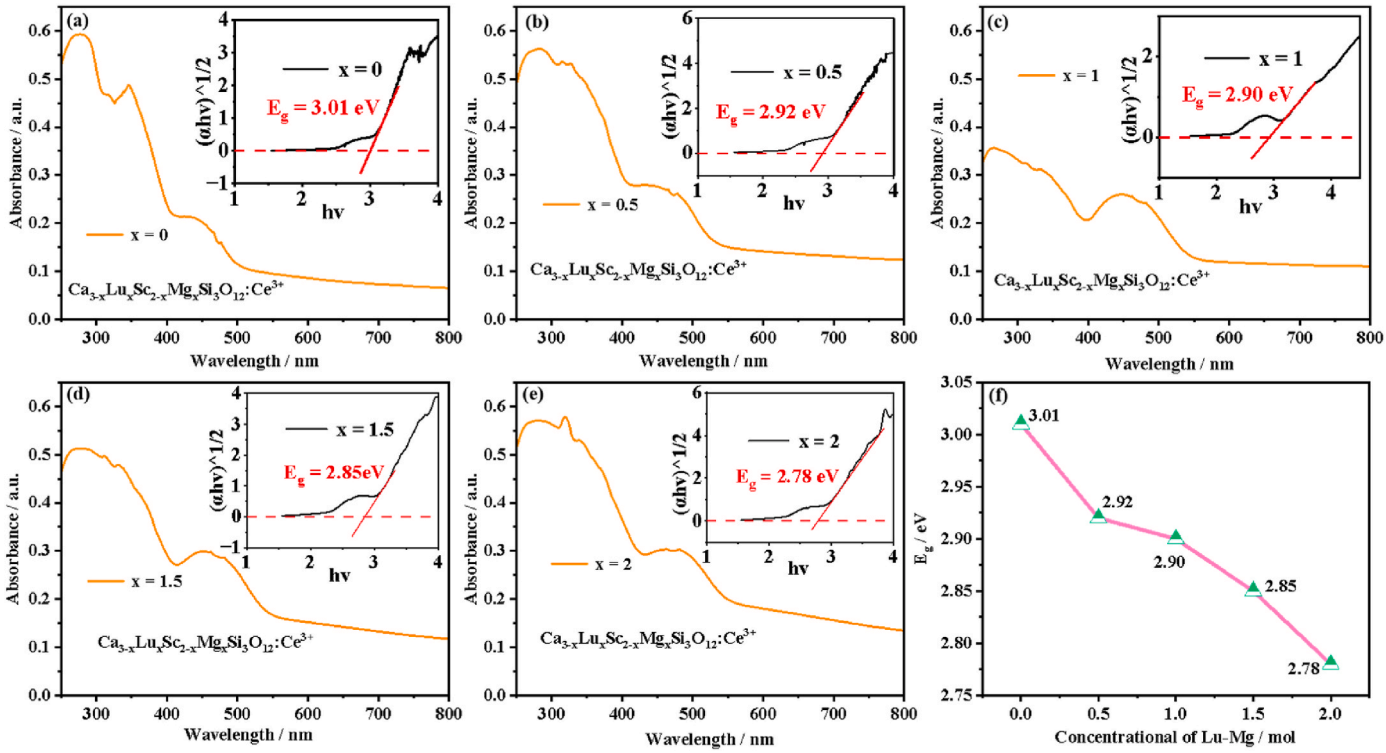

Fig. 9. (a)–(e) Diffuse reflectance spectra of CLSMS:Ce^{3+} materials (Inset is the calculated forbidden bandwidth), and (f) trend of the forbidden bandwidth.

the decay time of the CLSMS series samples at the other monitoring wavelengths. Comparison with Fig. 10(a) reveals that the increase of the monitoring wavelength increases the decay time of each sample, indicating that the sample has multiple luminescent centers. This is due to the random distribution of Ce^{3+} around Lu^{3+} and Ca^{2+} after the introduction of Lu–Mg, and the difference in the surrounding crystal field environment of Lu^{3+} and Ca^{2+} leads to the formation of multiple luminescent centers of Ce^{3+}.

The performance of the CLSMS:Ce^{3+} based LD device (λ_{ex} = 450 nm) is shown in Fig. 11. Fig. 11(a) shows the electroluminescence (EL)

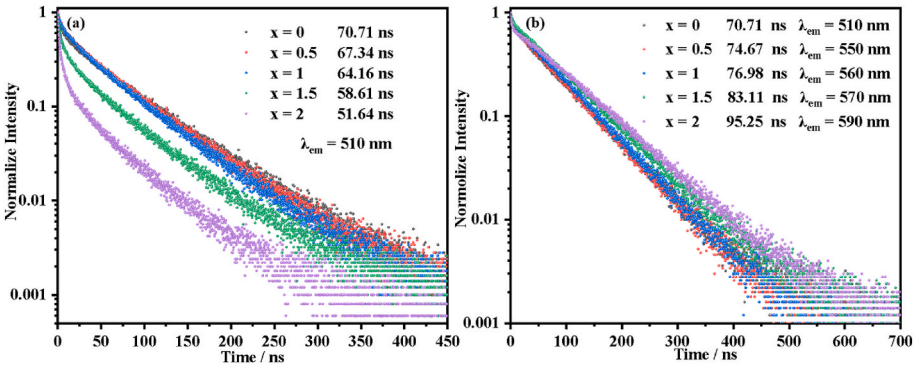

Fig. 10. The decay time curve of CLSMS:Ce^{3+} materia at (a) λ_{ex} = 510 nm and (b) the other monitoring wavelengths.

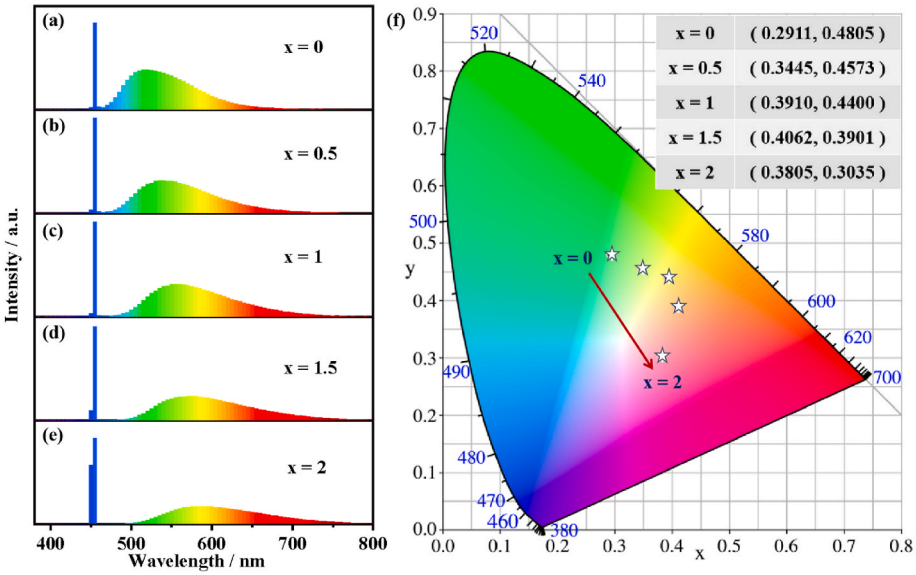

Fig. 11. (a) The measured EL spectra and (b) the corresponding of color coordinates of CLSMS:Ce^{3+} series materials.

spectra of the CLSMS:Ce^{3+} series material, with the corresponding chromaticity coordinates obtained by tracing the points, as shown in Fig. 11(b). It can be observed that the yellow and red components of the samples gradually increase and the cyan-green component gradually decreases as the concentration of Lu–Mg increases. The corresponding CIE coordinates also shift from (0.2911, 0.4805) to (0.3805,0.3035). In addition to this, as shown in Fig. 12, there is a significant decreasing trend in the CCT of the samples as the Lu–Mg concentration increased from 0 to 2. At the same time, the luminous flux and luminous efficacy of CLSMS:Ce^{3+} series samples under different input powers were measured, as shown in Fig. 12(c) and (d). It is clearly seen in the figure that with the increase of power in this power range, the overall luminous flux and luminous efficacy of the samples generally increased. Under the excitation of maximum input powers, the luminous efficacy of CLSMS:Ce^{3+} decreased with the increase of Lu–Mg concentration (Fig. 12(b)). In contrast, there is a moderate increase in color rendering index (CRI).

The two materials CSS:Ce^{3+} (x = 0) and CLMS:Ce^{3+} (x = 2) were compounded. The WLD properties of the composites are shown in Fig. 13, with detailed EL, CCT, CRI and CIE color coordinate parameters shown in Fig. 13(b). As can be observed by the EL, the color coordinates of the samples are close to standard white light and there is a moderate increase in CRI compared to the EL spectrum of YAG:Ce^{3+} in Fig. 13 (a). This is due to the fact that both the cyan spectral canyon and the red component of the sample are compensated for. Photographs of the WLD devices based on CSS:Ce^{3+}, CLMS:Ce^{3+} and composites are also shown in Fig. 13(c). It can be observed that the hues of the LD devices are cyan-green, orange-red and white respectively. In summary, CLSMS:Ce^{3+} is a promising fluorescent material for applications in LD lighting. It is potentially informative for the complement of cyan-green and red light.

4. Conclusion

In this paper, CLSMS:Ce^{3+} (x = 0, 0.5, 1, 1.5, 2) were successfully prepared by high temperature solid state reaction method and their luminescence properties were systematically investigated. On the basis of CSS:Ce^{3+}, different concentrations of Lu–Mg ions pairs were introduced in the matrix to replace Ca–Sc ions. By XRD analysis, the introduction of Lu–Mg ions caused the diffraction peaks of the samples to change gradually from the CSS phase to the YAG phase. The increase in Lu–Mg concentration leaded to a lower center of gravity of the 5d energy level and a decrease in the energy level difference. As a result, the highest emission peak position of the sample was red-shifted by 81 nm with increasing Lu–Mg concentration. In addition to this, the thermal stability of the phosphor gradually deteriorated with increasing Lu–Mg concentration from CSS to CLMS. At 423 K, the emission intensity of the samples decreased to 98.11 %, 94.13 %, 92.18 %, 81.96 % and 77.60 % of that at 298 K, respectively. The activation energy of the CLSMS:Ce^{3+} phosphor was calculated and the activation energy was reduced. And the color coordinates of the samples were calculated. The CLSMS:Ce^{3+} series of fluorescent materials and composites were LD encapsulated and the

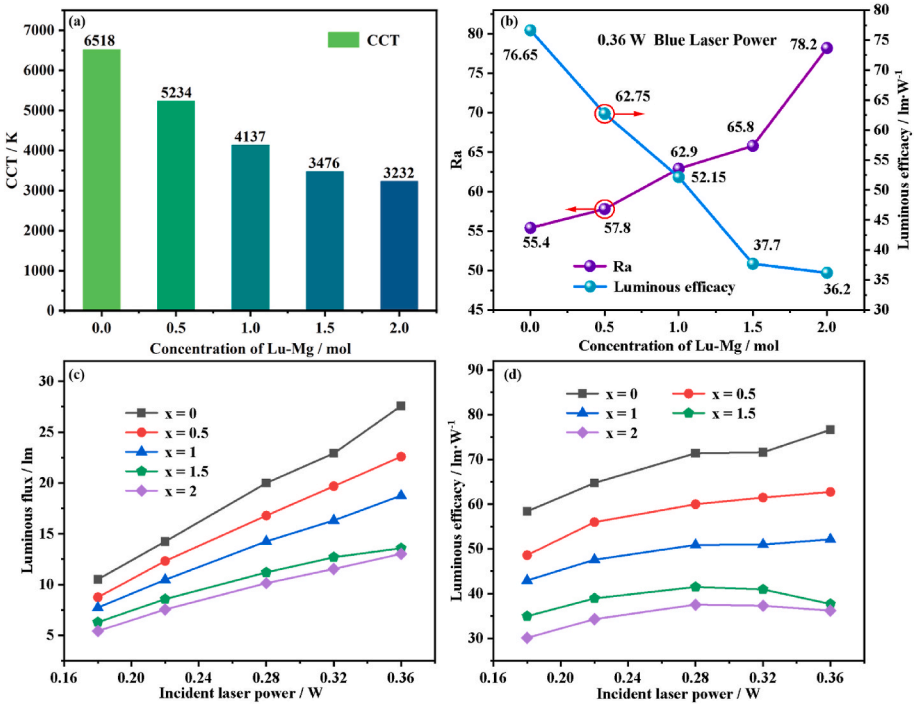

Fig. 12. (a) The CCT and (b) the trend diagram of color rendering index and luminous efficacy with the introduction of Lu–Mg, (c) luminous flux and (d) luminous efficacy of CLSMS:Ce^{3+} series materials at different powers (Optical Power: 80 mW).

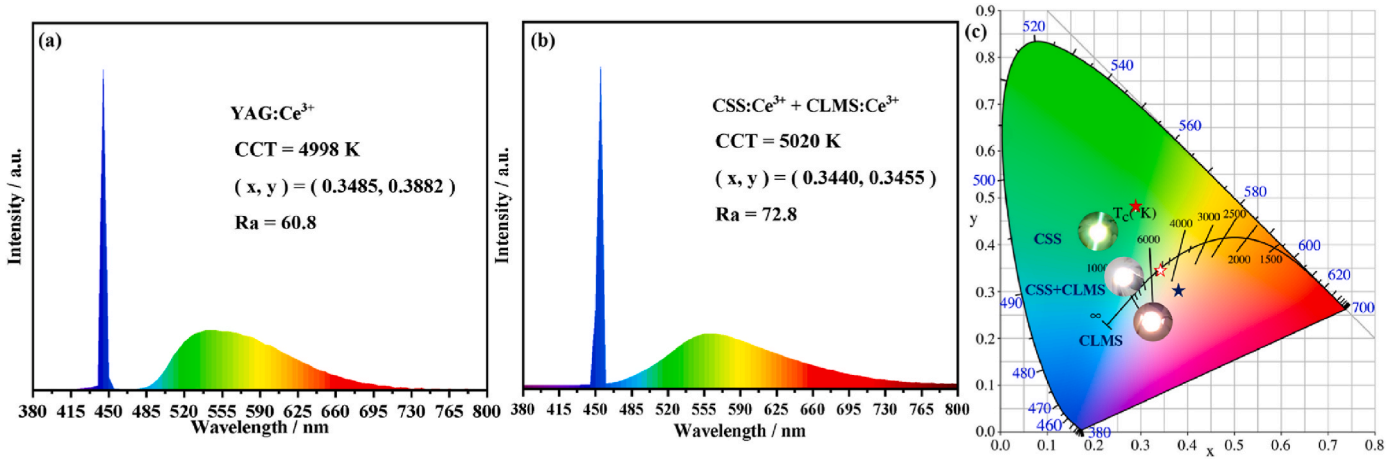

Fig. 13. (a) The measured EL spectra of YAG:Ce^{3+} (b) the measured EL spectra and (c) the corresponding of color coordinates of the CSS and CLMS composite.

color coordinates of the series of samples were found to gradually shift towards red light. The color coordinates of the composite prepared devices were (0.3440, 0.3455), close to the standard white light. The cyan spectral canyon and red light components of the samples were also compensated for. In conclusion, this study demonstrates that CLSMS:Ce^{3+} is a very promising fluorescent material. It is of potential reference value for the field of white LD lighting for complementing the cyan-green and red light components.

CRediT authorship contribution statement

Xin Li: Conceptualization, Data curation, Formal analysis, Investigation, Writing – original draft. **Yu Zhang:** Formal analysis, Investigation. **Hongrui Ren:** Formal analysis, Investigation. **Lunlong Xie:** Methodology, Validation. **Yinsheng Di:** Methodology, Validation. **Mengqing Han:** Methodology, Validation. **Zhaohui Bai:** Formal analysis, Supervision. **Quansheng Liu:** Supervision, Writing – review & editing. **Liangliang Zhang:** Writing – review & editing. **Jiahua Zhang:** Writing – review & editing.

Declaration of competing interest

We declare that we do not have any commercial or associative interest that represents a conflict of interest in connection with the work submitted. We declare that we have no financial and personal relationships with other people or organizations that can inappropriately influence our work.

Data availability

The data that has been used is confidential.

Acknowledgements

This work was supported by these projects, which are the National Natural Science Foundation of China (No. U22A20139) and the Education Department of Jilin Province (No. JJKH20210856KJ).

References

[1] J.Y. Tsao, M.H. Crawford, M.E. Coltrin, A.J. Fischer, D.D. Koleske, G. S. Subramania, G.T. Wang, J.J. Wierer, R.F. Karlicek, Toward smart and ultra-efficient solid-state lighting, Adv. Opt. Mater. 2 (9) (2014) 809–836.
[2] J.J. Wierer, J.Y. Tsao, D.S. Sizov, Comparison between blue lasers and light-emitting diodes for future solid-state lighting, Laser Photon. Rev. 7 (6) (2013) 963–993.
[3] C. Weisbuch, Review-on the search for efficient solid state light emitters: past, present, future, ECS J. Solid State Sci. Technol. 9 (1) (2020), 016022.
[4] F. Schütt, M. Zapf, S. Signetti, J. Strobel, H. Krüger, R. Röder, J. Carstensen, N. Wolff, J. Marx, T. Carey, M. Schweichel, M.I. Terasa, L. Siebert, H.K. Hong, S. Kaps, B. Fiedler, Y.K. Mishra, Z. Lee, N.M. Pugno, L. Kienle, A.C. Ferrari, F. Torrisi, C. Ronning, R. Adelung, Conversionless efficient and broadband laser light diffusers for high brightness illumination applications, Nat. Commun. 11 (1) (2020) 1437.
[5] J.J. Wiererjr, J.Y. Tsao, Advantages of III-nitride laser diodes in solid-state lighting, Phys. Status Solidi A 212 (5) (2015) 980–985.
[6] S.X. Li, L. Wang, N. Hirosaki, R.J. Xie, Color conversion materials for high-brightness laser-driven solid-state lighting, Laser Photon. Rev. 12 (12) (2018), 1800173.
[7] P. Hu, H. Ding, Y.F. Liu, P. Sun, Z.H. Liu, Z.H. Luo, Z.R. Huang, H.C. Jiang, J. Jiang, Recent progress of YAG:Ce^{3+} for white laser diode lighting application, Chin. J. Lumin. 41 (12) (2020) 1504–1528 (in Chinese).
[8] L. Chen, C.C. Lin, C.W. Yeh, R.S. Liu, Light converting inorganic phosphors for white light-emitting diodes, Materials 3 (3) (2010) 2172–2195.
[9] Z.G. Xia, Z.H. Xu, M.Y. Chen, Q.L. Liu, Recent developments in the new inorganic solid-state LED phosphors, Dalton Trans. 45 (28) (2016) 11214–11232.
[10] A.A. Serlur, W.J. Heward, M.E. Hannah, U. Happek, Incorporation of Si^{4+}-N^{3-} into Ce^{3+}-doped garnets for warm white LED phosphors, Chem. Mater. 20 (19) (2008) 6277–6283.
[11] P. Sun, P. Hu, Y.F. Liu, S. Liu, R. Dong, J. Jiang, H.C. Jiang, Broadband emissions from $Lu_2Mg_2Al_2Si_2O_{12}$:Ce^{3+} plate ceramic phosphors enable a high color-rendering index for laser-driven lighting, J. Mater. Chem. C 8 (4) (2020) 1405–1412.
[12] N. Khaidukov, Y. Zorenko, T. Zorenko, A. Iskaliyeva, K. Paprocki, Y. Zhydachevskii, A. Suchocki, R.V. Deun, M. Batentschuk, New Ce^{3+} doped $Ca_2YMgScSi_3O_{12}$ garnet ceramic phosphor for white LED converters, Phys. Status Solidi RRL (2017), 1700016.
[13] L.P. Jiang, X. Jiang, C.X. Wang, P. Liu, Y. Zhang, G.C. Lv, T. Lookman, Y.J. Su, Rapid discovery of efficient long-wavelength emission garnet:Cr NIR phosphors via multi-objective optimization, ACS Appl. Mater. Interfaces 14 (46) (2022) 52124–52133.
[14] V.P. Dotsenko, I.V. Berezovskaya, A.S. Voloshinovskii, B.I. Zadneprovski, N. P. Efryushina, Luminescence properties of Eu^{2+} and Ce^{3+} ions in calcium lithio-germanate Li_2CaGeO_4, Mater. Res. Bull. 64 (2015) 151–155.
[15] H.K. Park, J.H. Oh, H. Kang, J. Zhang, Y.R. Do, Hybrid 2D photonic crystal-assisted $Lu_3Al_5O_{12}$:Ce^{3+} ceramic-plate phosphor and free-standing red film phosphor for white LEDs with high color-rendering index, ACS Appl. Mater. Interfaces 7 (2015) 4549–4559.
[16] G.S. Han, Y.H. Song, D.H. Kim, M.J. Lee, D.G. Lee, S.H. Han, Y.J. Kim, M.K. Jung, D.H. Yoon, H.S. Jung, Green-emitting $Lu_3Al_5O_{12}$:Ce^{3+} phosphor as a visible light amplifier for dye-sensitized solar cells, RSC Adv. 5 (2015) 24737–24741.
[17] M.J. Lee, S.H. Park, Y.H. Song, E.K. Ji, U.B. Humayoun, D.B. Lee, D.H. Yoon, Fabrication of phosphor ceramic plate using green-emitting $Lu_3Al_5O_{12}$:Ce^{3+} phosphor for high power LEDs, Mater. Lett. 161 (2015) 708–711.
[18] B. Wang, R. Mi, Y. Liu, M. Yu, Z. Huang, M. Fang, Identification of dual luminescence centers from A single site in A, novel blue-pumped $Ca_3Sc_2Ge_3O_{12}$:Ce^{3+} phosphor, Dalton Trans. 48 (2019) 11791–11802.
[19] W. Zhang, L. Jiang, L. Cheng, S. Xu, C. Wang, S. Zhu, X. Mi, X. Zhang, X. Liu, Weak thermal quenching of the luminescence in $Y_{2.94-x}Lu_xAl_4GaO_{12}$:$0.06Ce^{3+}$ green phosphor for white light emitting diodes, Ceram. Int. 45 (2019) 23451–23457.
[20] J. Liang, B. Devakumar, L.L. Sun, S.Y. Wang, Q. Sun, X.Y. Huang, Full-visible-spectrum lighting enabled by an excellent cyan-emitting garnet phosphor, J. Mater. Chem. C 8 (2020) 4934.
[21] L.N. Cao, W. Li, B. Devakumar, N. Ma, X.Y. Huang, A.F. Lee, Full-spectrum white light-emitting diodes enabled by an efficient broadband green-emitting $CaY_2ZrScAl_3O_{12}$:Ce^{3+} garnet phosphor, ACS Appl. Mater. Interfaces 14 (4) (2022) 5643–5652.
[22] L.N. Cao, Z. Xu, J.M. Chan, B. Devakumar, X.Y. Huang, Realizing full-spectrum LED lighting with a bright broadband cyan-green-emitting $CaY_2ZrGaAl_3O_{12}$:Ce^{3+} garnet phosphor, J. Lumin. 263 (2023), 120015.
[23] Y.C. Jia, Y.J. Huang, Y.H. Zheng, N. Guo, H. Qiao, Q. Zhao, H.P. You, Color point tuning of $Y_3Al_5O_{12}$:Ce^{3+} phosphor via Mn^{2+}-Si^{4+} incorporation for white light generation, J. Mater. Chem. 22 (30) (2012) 15146–15152.
[24] L.P. Jiang, X. Jiang, Y. Zhang, C.X. Wang, P. Liu, G.C. Lv, Y.J. Su, Multiobjective machine learning-assisted discovery of a novel cyan-green garnet:Ce phosphors with excellent thermal stability, ACS Appl. Mater. Interfaces 14 (2022) 15426–15436.
[25] H. Ji, L. Wang, M.S. Molokeev, N. Hirosaki, R.J. Xie, Z. Huang, Z. Xia, O.M. Ten Kate, L. Liu, V.V. Atuchin, Structure evolution and photoluminescence of $Lu_3(Al,Mg)_2(Al,Si)_3O_{12}$:$Ce^{3+}$ phosphors: new yellow-color converter for blue LED-driven solid state lighting, J. Mater. Chem. C 4 (2016) 6855–6863.
[26] M. Liang, J. Xu, Y.C. Qiang, H.J. Kang, L.L. Zhang, J. Chen, C. Liu, X.B. Luo, Y. Li, J. J. Zhang, Ouyang. Ce^{3+} doped $BaLu_2Al_2Ga_2SiO_{12}$-A novel blue-light excitable cyan-emitting phosphor with ultra-high quantum efficiency and excellent stability for full-spectrum white LEDs, J. Rare Earths 39 (2020) 1031.
[27] C. He, H. Ji, Z. Huang, T. Wang, X. Zhang, Y. Liu, M. Fang, X. Wu, J. Zhang, X. Min, Red-shifted emission in $Y_3MgSiAl_3O_{12}$:Ce^{3+} garnet phosphor for blue light-pumped white light-emitting diodes, J. Phys. Chem. C 122 (2018) 15659–15665.
[28] Z. Pan, Y. Xu, Q. Hu, W. Li, H. Zhou, Y. Zheng, Combination cation substitution tuning of yellow-orange emitting phosphor $Mg_2Y_2Al_2Si_2O_{12}$:Ce^{3+}, RSC Adv. 5 (2015) 9489–9496.
[29] X. Gong, J. Huang, Y. Chen, Y. Lin, Z. Luo, Y. Huang, Novel garnet-structure $Ca_2GdZr_2(AlO_4)_3$:Ce^{3+} phosphor and its structural tuning of optical properties, Inorg. Chem. 53 (2014) 6607–6614.
[30] X. Ding, G. Zhu, W. Geng, Q. Wang, Y. Wang, Highly efficient cyan-emitting garnet phosphor $Ca_3Hf_2SiAl_2O_{12}$:xCe^{3+} for solid state white lighting, CrystEngComm 17 (2015) 3235–3242.
[31] I. Levchuk, A. Osvet, C.J. Brabec, M. Batentschuk, A. Shakhno, T. Zorenko, Y. Zorenko, Micro-powder $Ca_3Sc_2Si_3O_{12}$:Ce^{3+} silicate garnets as efficient light converters for WLEDs, Opt. Mater. 107 (2020), 109978.
[32] J.M. Herzog, D. Witkowski, D.A. Rothamer, Characterization of Ce:CSSO, Pr:CSSO, and co-doped Ce, Pr:CSSO phosphors for aerosol phosphor thermometry, Meas. Sci. Technol. 32 (2021), 054008.
[33] P.P. Lohea, D.V. Nandanwara, P.D. Belsareb, S.V. Moharil, Cyan emitting $Ca_3Sc_2Si_{1.5}Ge_{1.5}O_{12}$:$Ce^{3+}$ phosphor with 10.4 ns lifetime, J. Lumin. 216 (2019), 116744.
[34] A. Katelnikovas, T. Bareika, P. Vitta, T. Jüstel, H. Winkler, A. Kareiva, A. Žukauskas, G. Tamulaitis, $Y_{3-x}Mg_2AlSi_2O_{12}$:Ce^{3+} Phosphors-Prospective for warm-white light emitting diodes, Opt. Mater. 32 (2010) 1261–1265.
[35] J. Zhong, W. Zhuang, X. Xing, R. Liu, Y. Li, Y. Liu, Y. Hu Synthesis, Crystal structures, and photoluminescence properties of Ce^{3+}-doped $Ca_2LaZr_2Ga_3O_{12}$:Ce^{3+} new garnet green-emitting phosphors for white LEDs, J. Phys. Chem. C 119 (2015) 5562–5569.
[36] G. Li, Y. Tian, Y. Zhao, J. Lin, Recent progress in luminescence tuning of Ce^{3+} and Eu^{3+}-activated phosphors for pc-WLEDs, Chem. Soc. Rev. 44 (2015) 8688–8713.
[37] M. Shang, J. Fan, H. Lian, Y. Zhang, D. Geng, J. Lin. A double substitution of Mg^{2+}-Si^{4+}/Ge^{4+} for $Al^{3+}_{(1)}$-$Al^{3+}_{(2)}$ in Ce^{3+}-doped garnet phosphor for white LEDs, Inorg. Chem. 53 (2014) 7748–7755.
[38] A. Katelnikovas, H. Bettentrup, D. Uhlich, S. Sakirzanovas, T. Jüstel, A. Kareiva, Synthesis and optical properties of Ce^{3+}-doped $Y_3Mg_2AlSi_2O_{12}$ phosphors, J. Lumin. 129 (2009) 1356–1361.
[39] M.S. Kishore, N.P. Kumar, R.G. Chandran, A.A. Setlur, Solid solution formation and Ce^{3+} luminescence in silicate garnets, Electrochem. Solid State Lett. 13 (2010) J77.
[40] G. Feng, W. Jiang, J. Liu, C. Li, Q. Zhang, L. Miao, Q. Wu, Synthesis and luminescence properties of Al_2O_3@YAG:Ce^{3+} core-shell yellow phosphor for white LED application, Ceram. Int. 44 (2018) 8435–8439.
[41] G. Gu, W. Xiang, C. Yang, W. Fan, Y. Lv, Z. Zhang, X. Liang, A novel single-component white-emitting Tb and Mn Co-doped large-sized $Y_3Al_5O_{12}$:Ce^{3+} single crystal for white LED, Sci. Adv. Mater. 8 (2016) 1354–1360.
[42] Y. Du, C. Shao, Y. Dong, Q. Yang, Electroluminescent properties of WLEDs with the structures of Ce:YAG single crystal/blue chip and $Sr_2Si_5N_8$:Eu^{2+}/Ce:YAG single crystal/blue chip, J. Disp. Technol. 12 (2016) 323–327.
[43] B.Y. Zhao, X. Liang, Z. Chen, C. Xie, L. Luo, Z. Zhang, W. Xiang, Studies on optical properties and Ce^{3+} concentration of Ce^{3+}:YAG single crystal for WLEDs, Chem. J. Chin. Univ. 25 (2014) 230–236.
[44] J.M. Hu, R. Wang, C.T. Wang, C. Zhang, Y.Y. Wang, X ray diffraction model of crystal and general derivation of bragg equation, Coll. Phys. 34 (3) (2015) (in Chinese).
[45] X. Li, C. Zhang, J. Chen, Q.S. Liu, Z.H. Bai, X.L. Liu, X.Y. Mi, Cr^{3+} ions improving the spectral properties of YAG: Ce^{3+} luminescent ceramics for white LD lighting, Ceram. Int. 49 (2023) 5489–5495.
[46] P. Dorenbos, J. Andriessen, C.W.E. van Eijk, $4f_{n-1}5d$ centroid shift in lanthanides and relation with anion polarizability, covalency, and cation electronegativity, J. Solid State Chem. (1–2) (2003) 133–136.
[47] F. Pan, M. Zhou, J. Zhang, X. Zhang, J. Wang, L. Huang, X. Kuang, M. Wu, A double substitution induced tunable luminescent properties of $Ca_{3-x}Y_xSc_{2-x}Mg_xSi_3O_{12}$:$Ce^{3+}$ phosphors for white LEDs, J. Mater. Chem. C 4 (2016) 5671–5678.
[48] S. Bhushan, M.V. Chukichev, Temperature dependent studies of cathodoluminescence of green band of ZnO crystals, J. Mater. Sci. Lett. 7 (1988) 319–321.